Laurin, J., Uličný, D., Waltham, D., Toman, P., Warsitzka, M., Sageman, B. B., 2023. Contrasting response of sea-level change to orbital eccentricity in greenhouse and icehouse climates. *Earth and Planetary Science Letters*, 622, 118421, doi:10.1016/j.epsl.2023.118421

Contrasting response of sea-level change to orbital eccentricity in greenhouse and icehouse climates

Jiří Laurin[1], David Uličný[1], Dave Waltham[2], Petr Toman[3], Michael Warsitzka[1], Bradley B. Sageman[4]

[1] *Institute of Geophysics AS CR, v.v.i., Boční II/1401, 141 31 Prague, Czech Republic*

[2] *Department of Earth Sciences, Royal Holloway, University of London, Egham, Surrey TW20 0EX, UK*

[3] *Institute of Applied Mathematics and Information Technologies, Charles University, Albertov 6, 128 43, Prague, Czech Republic*

[4] *Department of Earth and Planetary Sciences, Northwestern University, Evanston, Illinois 60208-3130, USA.*

Corresponding author: laurin@ig.cas.cz

ABSTRACT

Climate-controlled changes in eustatic sea level (ESL) are linked to transfers of water between ocean and land, thus offering a rare insight into the past hydrological cycle. In this study, we examine the timing and phase of Milankovitch-scale ESL cycles in the peak Cretaceous greenhouse, the early Turonian (~93-94 million years, Myr, ago). A high-resolution astronomical framework established for the Bohemian Cretaceous Basin (central Europe) suggests a ~400-kyr pace and a distinct asymmetry of interpreted ESL cycles. The rising limbs of ESL change constitute only 20-30% of the cycle, and are encased entirely within the falling phase of the 405-kyr eccentricity; the intervening ESL falls (≤6 m in magnitude) are more protracted, starting within 70 kyr prior to the eccentricity minima and culminating ~60 kyr after the 405-kyr eccentricity maxima. Despite similarities to the sawtooth shape of ~100-kyr glacioeustatic oscillations of the Late Pleistocene, the time scales and phasing are unparalleled in the Pleistocene icehouse. A similar, 405-kyr pace is

found in ice-volume variations of the early Miocene, but the timing of glacioeustatic change relative to eccentricity forcing is incompatible with the phase of greenhouse sea-level oscillations. The phasing points to major differences in the geographic location and insolation sensitivity of the key hydrological reservoirs under icehouse and greenhouse regimes. The inferred structure of greenhouse eustasy points to low- or middle-latitude water storage, likely aquifers, that charge (expand) with rising seasonality variations and discharge (contract) with declining seasonality amplitudes on the 405-kyr scale. The net volume of water transferred on these time scales is within 2.2 x10^6 km^3, equivalent to ≤10 % of the present-day storage in the uppermost 2 km of continental crust; potential additive interference with steric eustasy, proportionally relevant during greenhouse regimes, could reduce the volumes required for continental storage.

1. INTRODUCTION

Storage of water in continental ice and aquifers are the two most efficient mechanisms capable of producing global (eustatic) sea-level change on relatively short, 10's to 100's thousand-year (kyr) time scales. The primary forcing of these glacio-eustatic and aquifer-eustatic fluctuations is linked to astronomically controlled changes in insolation (Milankovitch 1941) via arrays of climate responses and feedbacks involving the carbon cycle, circulation of the ocean and atmosphere, and vegetation changes. The causal mechanisms are relatively well understood for the most recent geological history (e.g., Imbrie et al. 1992; Ai et al. 2020), but become increasingly blurred towards the deeper past, in particular beyond ~50 Myr ago. One of the sources of this uncertainty is the lack of reliable astronomical solution (Laskar et al. 2011; Zeebe and Lourens 2019) that would provide a reference frame against which to define the phasing and lead/lag relationships between the astronomical forcing and climate change. Stratigraphic correlation and radioisotopic dating impart additional uncertainties. Taking the interval 90-100 Myr ago as an example, even the most stable astronomical term - the 405-kyr eccentricity, which is related to the secular interaction of orbital perihelia of Venus and Jupiter (g_2-g_5; Laskar et al. 2004, 2011; Laskar 2020) - has a possible deviation of ±80 kyr (Laskar et al. 2011). When tied to high-precision U-Pb ages, whose uncertainty equals or exceeds ±140 kyr (Gradstein et al. 2020), the combined uncertainty reaches the duration of the entire 405-kyr cycle, thus

rendering any phase evaluation impossible. It is these deep-time, weakly constrained intervals that include the most typical greenhouse regimes of Earth history that are characterized by warm and equable climates, reduced latitudinal temperature gradients and no or limited ice cover at the poles (e.g., Pagani et al. 2014). Some of the most persistent uncertainties related to the greenhouse regime, including the origin of sea-level fluctuations and the unsettled question of greenhouse glacioeustasy (e.g., discussions in Ray et al. 2019; Plint et al. 2022) can be attributed to the weakly constrained astronomical forcing. Further progress must rely on empirical data and requires pristine records of both astronomical cyclicity (typically preserved in open-marine settings) and sea-level change (best recorded in nearshore and coastal depositional systems).

Here we use an exceptionally well-preserved astronomical cyclicity from offshore and hemipelagic facies of the Bohemian Cretaceous Basin (central Europe) that provides a robust framework of eccentricity phasing across a ~1 Myr interval overlapping with the mid-Cretaceous thermal maximum (early to early middle Turonian; Fig. 1). Wireline logs from closely spaced boreholes make it possible to link this astronomical framework in high resolution (<20 kyr) to the nearshore record of transgressive-regressive shoreline movements and sea-level change. The results are compared with published sea-level curves for the early Miocene (Liebrand et al. 2017) and Late Pleistocene (Spratt and Lisiecki 2016), which serve as reference examples of eustatic regimes controlled by uni-polar (Antarctic) and bi-polar glaciations, respectively. Differences in the phasing of sea-level change relative to the astronomical forcing suggest contrasting mechanisms and sources of sea-level variability under greenhouse and icehouse climates.

2. DATA AND METHODS

2.1 Terminology

This paper aims to interpret the timing of eustatic sea-level changes, which are understood as global-scale variations in the mean height of the ocean surface relative to the center of the Earth. They can be induced either by a change in the volume of ocean water or by a change in the capacity of ocean basins. Here, the interpretation of eustatic sea-level change relies on its role in controlling nearshore facies and stratal geometries through changes in the accommodation space or relative sea level, which refers to the vertical dimension

between the local sea surface and the underlying basement. In this paper, the term "sea-level change" refers primarily to "relative sea-level change" unless otherwise noted.

2.2 Data

A record of greenhouse sea-level change that can be linked in high resolution to a robust astronomical framework is examined in shallow-marine deposits of the western part of the Bohemian Cretaceous Basin (Fig. 2). The basin fill consists of sand-dominated, deltaic and shoreface siliciclastics that are sourced from a relatively small source area to the north-east (the Western Sudetic Island) and reworked by along-strike (northwest and southeast oriented) tidal currents (Mitchell et al. 2010). Progradational and retrogradational patterns of these nearshore siliciclastics define major, basinwide sequences labelled TUR1 and TUR2 in the lower Turonian and TUR3 through TUR7 in the middle and upper Turonian. The distal, southwestern parts of the basin are occupied by fine-grained siliciclastics, mostly calcareous mudstones and hemipelagic marlstones; these strata are the source of precession-scale astrochronology (see below). Details on the three-dimensional geometry of the basin fill can be found in Uličný et al. (2009), with additional refinements in Uličný et al. (2014) and Laurin et al. (2021).

This study focuses on the lower Turonian to lowermost middle Turonian interval represented by sequences TUR1, TUR2 and lower part of TUR3. The bulk of the available data comes from the subsurface, consisting mainly of wireline gamma-ray and resistivity logs. Two cores located in a distal offshore position (4523-A and 4530-A; Fig. 2) were previously examined for lithofacies, major and minor element composition and carbon-isotope ratios (Laurin et al. 2021). A representative cross-section was constructed from the northern basin margin, approximately 10 km basinward from the uplifted Western Sudetic Island towards the southwest and west-southwest, i.e., parallel to oblique to the depositional dip (Figs. 2, 3; Supplementary Figures S1 and S2). The trace of this cross-section was adjusted to follow the highest density of borehole data in order to obtain an accurate, high-resolution correlation. The dense framework of well logs makes it possible to study the facies and geometric relationships, delineate key sequence stratigraphic surfaces and correlate the astrochronological framework from offshore rhytmites to nearshore sequences.

Numerical representation of the transgressive-regressive movements is achieved through tracing siliciclastic facies along the proximal-distal transect with normalized gamma-ray logs (where pure sand = 0 and pure mud = 1; Fig. 3). The shoreline cannot be identified in the subsurface data. Therefore, "shoreface envelope" defined by the trajectory of >30% sand contents in the normalized gamma-ray logs is used here to approximate transgressive and regressive changes of the shoreline.

2.3 Delineation of sequences, surfaces and tracts

Progradational and retrogradation arrangements of siliciclastic facies provide the primary criterion for delineating regressive and transgressive tracts, respectively, in the study interval (Uličný et al. 2009). Each sequence is bracketed below and above by a surface of maximum transgression, which represents the turnaround from retrogradational to progradation facies stacking. Sequences TUR1 through TUR3 are therefore equivalent to "genetic sequences" *sensu* Galloway (1989). No distinct geometric downlap or surface of sediment starvation is associated with the maximum flooding at the bases of TUR2 and TUR3, owing to a relatively short duration of the transgressive phases (see below) and generally high fluxes of fine grained siliciclastics throughout the study interval. Sequence TUR1 is distinct, as it represents the first shoreface progradation across a large-scale transgressive interval related to the Cenomanian/Turonian tectonoeustatic sea-level rise (Hancock and Kauffman 1979). The base of the regressive tract of sequence TUR1 is placed at the onset of first shoreface siliciclastics in the most proximal part of the basin, approximately 120 kyr after the Cenomanian-Turonian boundary (Fig. 3; Supplementary Figure S1). In each sequence, the top of the regressive tract is defined by the maximum basinward extent of shoreface siliciclastics, labelled as maximum regression in this paper. This surface marks the very onset of facies backstepping, but occurs some distance (equivalent here to 90-100 kyr) beneath an abrupt landward shift in facies, which could be considered the initial flooding surface in sequence stratigraphic models (cf. Van Wagoner et al. 1988). The maximum basinward extent of shoreface siliciclastics provides a suitable reference level for this study, because it is both readily recognizable in well-log cross sections (Fig. 3) and numerical models (section 2.7), and its correlation to astronomical time scale is not hindered by non-deposition or winnowing (as is often the case for the initial flooding surfaces). Evidence for subaerial unconformities or Type-1 sequence boundaries

sensu Van Wagoner et al. (1988) are not recognized (see Uličný et al. 2009 for discussion), but some of the regressive tracts exhibit a distinct change from progradational and aggradational facies arrangement that resembles Type-2 sequence boundary in the original sequence stratigraphic models (Fig. 3).

2.4 Age model

A floating astrochronology for this study is based on precession-scale cyclicity of the offshore succession, which covers the entire lower Turonian (sequences TUR1 and TUR2) and the lowermost part of the middle Turonian (the top of sequence TUR2 and lower part of sequence TUR3). Spectral estimates for the astronomical interpretation were obtained from resistivity logs (primarily J-719 670 and J-650 704) and from one greyscale dataset (core 4523-A). Details on spectral estimates and construction of the astronomical time scale are provided in Laurin et al. (2021); see also section 2.5. The astronomical framework consists of 51 correlation markers or age control points, labelled "1a" through "43". Their stratigraphic position is indicated in Figure 3 and in a detailed correlation panel in Supplementary materials, Figure S1. The floating ages and uncertainties of these age control points are provided in Supplementary materials, Table S1.

The uppermost part of the study interval could not be linked to a high-resolution astrochronology due to reduced sedimentation rates and noisy time series in the regressive tract of sequence TUR 3. The time scale for middle and upper parts of sequence TUR 3 is adopted from the reference borehole Bch-1 (Laurin et al. 2015; Uličný et al. 2014; Supplementary Table S2). This part of the age model, however, relies on a linear interpolation, which introduces an increased potential for errors, and lacks an independent means of phase interpretation. Sequence TUR3 is therefore not evaluated and discussed in detail; the main focus of this study is sequences TUR1 and TUR2.

2.5 Astronomical solution

The uncertainty of astronomical tuning targets increases with increasing age (Berger et al. 1992; Waltham 2015); as a result, Myr-scale astronomical terms, which control the amplitude and frequency modulations of short-term (e.g., precessional) tuning targets become unpredictable beyond approximately 58 Myr ago (Laskar et al. 2011; Zeebe and Lourens 2019). Hence, the early Turonian astrochronology should not be based on tuning to

any particular segment of astronomical solutions. A metronomic time scale based on counting of precessional cycles offers an alternative approach, which, however, also requires a theoretical template to identify possible missing beats at eccentricity minima. To cope with these limitations, Laurin et al. (2021) selected a long, 10-Myr interval of the astronomical solution La2010d (Laskar et al. 2011) and compared the observed, precession-scale cyclicity with every segment of this interval that exhibited a compatible eccentricity-scale modulation. This approach made it possible to estimate the uncertainty related to Myr-scale modulation of the precessional tuning target and develop a floating age model without depending on a particular astronomical solution for the study interval. Additional details are provided in Laurin et al. (2021).

2.6 Eccentricity phasing

The phases of orbital eccentricity, i.e., the timing of maxima and minima of ~100-kyr and 405-kyr cycles, have been interpreted primarily from the amplitude modulation of well-preserved precessional cycles (Laurin et al. 2021). In this study we focus on the 405-kyr cyclicity, which is comparable in its scale to major depositional sequences TUR1 and TUR2. The timing and uncertainty of 405-kyr eccentricity extremes is adopted from the "nominal" age model of Laurin et al. (2021), and presented in Figure 3 as a tuned, 405-kyr cosine metronome (Laskar 2020). The uncertainty of the floating 405-kyr phase relative to the key sequence stratigraphic surfaces is estimated as ±52 to ±66 kyr (2σ); Table 1. An additional uncertainty is associated with the location of the Cenomanian-Turonian boundary (Tab. 1; Laurin et al. 2021). The 'absolute' age and formal chronostratigraphic context are, however, of secondary importance as this study targets the relative timing of eccentricity cycles with respect to the record of sea-level change. The chronostratigraphic uncertainty is therefore not included in further discussion.

2.7 Two-dimensional stratigraphic modeling

The transformation of eustatic sea-level change to nearshore stratigraphy is a non-linear process involving, in particular, the effects of subsidence, sediment distribution and depositional topography (Supplementary Figure S3). Here we attempt to approximate this transformation using two-dimensional, forward numerical modeling of siliciclastic sedimentation. The model - ShamFlu2D - is a development of SedTec2000 described in

Boylan et al. (2002). The key updates include a simplified, geometric simulation of the fluvial depositional system and the incorporation of user-defined variability in the input sediment fluxes (D. Waltham and P. Toman, this study; for details see Supplementary materials, Text S1 and Table S3).

To infer the phases of eustatic sea-level maxima and minima from transgressive-regressive shoreline movements, we employ an inverse approach using a series of sensitivity tests in which the input parameters are allowed to vary in ranges constrained by the lower Turonian stratigraphy. Fine-grained and coarse-grained siliciclastic fluxes are estimated from a restored cross section (Fig. 3) and the background accommodation, which accounts for the sum of subsidence, isostasy, compaction and long-term eustasy, is quantified using decompaction of the proximal (shallowest) part of the study interval (see section 2.8). Astronomical-scale sea-level oscillations are modelled using sinusoidal curves the amplitudes of which vary from 1 m to 10 m. Surfaces of maximum flooding and maximum regression, which are readily recognizable in both the model output and real stratigraphy, are compared with the timing of maxima and minima in the input sea-level curve. The relative timing then makes it possible to quantify the degree of phase distortion involved in the depositional system and to trace back the phase of eustatic sea-level forcing from the observed transgressive-regressive change (Fig. 5; section 3.3).

2.8 Subsidence analysis, decompaction

The sum of tectonic subsidence, isostatic adjustment of the crust to sediment and water load, compaction of the underlying sediment and long-term eustasy produces the background accommodation, which is supplied as one of the input parameters to stratigraphic models (section 2.7) and estimates of the magnitude of short-term sea-level fluctuations (section 3.4). In this study, the long-term eustasy is lumped with tectonic subsidence and the basement response because its effect on the local stratigraphy cannot be distinguished and quantified separately. The calculation follows the approach presented by Allen and Allen (2013) according to which the present-day thickness of each sedimentary layer is restored to its initial depositional porosity and thickness (decompacted); a detailed description of the decompaction procedure is provided in the Supplementary materials, Text S2 and Table S4. The approach is applied to borehole 072507, which provides a complete profile of the proximal part of the study interval (Supplementary materials,

Figures S1 and S4); the sediment surface at this proximal site remained close to sea level for most of the late Cenomanian through middle Turonian, thus minimizing the uncertainty due to changes in local bathymetry.

3. RESULTS

3.1 Lower Turonian sequences; time scales, phasing and accommodation rates

Transgressive-regressive changes of the lower Turonian to lowermost middle Turonian interval are linked to a precession-scale astronomical framework that has been inferred from cyclic variations in the lithology of offshore and hemipelagic strata (section 2.4). The astronomical rhythms are defined by changes in the proportion of fine grained siliciclastics (clay vs. silt contents) and carbonate, although the detailed interplay and origin of these lithological components remains poorly understood due to scarcity of core data (two cores recovered recently, 4523-A and 4530-A, are located at the edge of the type area of the rhythmic succession; Laurin et al. 2021). Importantly, the rhythmic succession provides a series of distinct correlation markers that can be traced in well logs to the immediate vicinity of the nearshore depocenter of coarse-grained siliciclastics, thus providing a high-resolution framework to the nearshore record of shoreline movements and sea-level change. Despite the proximity and local interfingering of the correlation markers with nearshore siliciclastics (Fig. 3), the offshore rhythmites do not exhibit any distinct lateral trend in the internal structure and amplitudes towards the nearshore setting (Supplementary materials, Fig. S1). This feature suggests a degree of decoupling of depositional processes along the depositional dip, between the offshore and nearshore depositional systems. Whereas the nearshore siliciclastics represent a proximal record of sea-level change and sediment input from the adjacent land, the offshore rhythmites were sensitive to changes in the along-strike currents and their impact on sediment redistribution and biogenic (carbonate) production. This decoupling is further highlighted by differences in the time scales of lithological variability: whereas the offshore system is paced by precessional cycles with a subordinate 100-kyr and weak 400-kyr cyclicities, the coarse-grained siliciclastics evolved at a much slower pace, in a pattern similar to the 400-kyr eccentricity as shown below. This distinction suggests that the offshore record of astronomical cyclicity can be applied as an independent template for high-resolution

chronology and phasing of the transgressive-regressive changes. In the following paragraphs, we apply the astronomical framework to sequences TUR1 and TUR2.

A detailed well-log correlation along proximal-distal transect suggests that the base of regressive systems tract of sequence TUR1 occurs between the age control points “2b3” and “3” (Fig. 3; Supplementary materials, Fig. S1). The maximum transgressive surface separating sequences TUR1 and TUR2 is bracketed by markers “22” and “23” and the maximum transgression capping sequence TUR2 is constrained by the age control points “38” and “39”. According to the astronomical time scale, the interval of sequences TUR1 and TUR2 represents 842 ±49 (2σ) kyr, with sequence TUR1 accounting for 459 ±44 (2σ) kyr and sequence TUR2 spanning 383 ±48 (2σ) kyr (combined uncertainties including uncertainty of the age model and uncertainty of the timing of key surfaces relative to the age control points; Supplementary materials, Tab. S1). The sequence-stratigraphic surfaces and tracts exhibit a systematic timing within the 405-kyr framework, with the maximum transgressive surfaces postdating 405-kyr maxima by 54 ±66 to 110 ±52 kyr (2σ) and regressive maxima coinciding with the 405-kyr maxima within ±60 kyr (Tab. 1; Fig. 5). These data point to a possible control by the 405-kyr cycle of orbital eccentricity. The periodicity has not been confirmed by spectral estimates due to a short time span of the study interval and a pronounced trend in the lower-middle Turonian shoreface progradation. However, analysis of the bulk Turonian shoreface envelope shows a prominent power-spectral and F-test significance maxima in the 405-kyr band (>99.99% F-test score; Supplementary materials, Fig. S5), in support of the above hypothesis.

The temporal structure of sequences TUR1 and TUR2 suggests a distinct asymmetry of transgressive-regressive cycles, with the transgressive tracts accounting for only 23-25% of the sequence duration. Superimposed upon these large-scale changes are subordinate fluctuations in the extent of shoreface siliciclastics, possibly reflecting ~100-kyr and shorter astronomical cycles (Supplementary materials, Figs. S1 and S2). The small amplitude and a limited correlatability between boreholes, however, prevents a detailed evaluation and attribution to sea-level change.

Finally, the astronomical time scale provides a temporal framework for the decompaction procedure and makes it possible to estimate the long-term rate of accommodation space creation, or the product of tectonic subsidence, long-term eustasy,

isostasy and compaction (section 2.8; Supplementary materials, Text S2). The decompaction procedure was applied to a broader interval (~1.15 Myr) in order to include the top of shallow-water Cenomanian siliciclastics and thus eliminate the bathymetric component (as both bottom and top of the decompacted interval formed at or close to zero water depth). Dividing the backstripped thickness of this interval by the estimated duration gives the mean rate of 158 m/Myr (Supplementary materials, Tab. S4). An uncertainty of ±7 m/Myr (2σ) is introduced from the age model (Supplementary materials, Tab. S1). We further assume that a possible deviation of the decompacted thickness is within ±10%, adding an uncertainty of ±16 m/Myr (maximum deviation), and resulting in a combined uncertainty of ±17 m/Myr (2σ; summation of quadrature). From the above estimate, tectonic subsidence alone accounts for 92 ±10 m/Myr.

3.2. Origin of lower Turonian sequences

The lower Turonian sequences TUR1 and TUR2 record transgressive-regressive cycles that could be related to relative sea-level change or merely to fluctuations in sediment delivery into the basin (sea-level-dominated vs. supply-dominated scenarios; cf. Thorne and Swift 1991). Direct evidence for relative sea-level falls in the form of, for example, fluvial incision (e.g., Van Wagoner et al. 1988) or detached shorefaces (e.g., Plint 1988) should not be expected because of the relatively rapid subsidence of the depocenter (~160 m/Myr) and the limited rates of greenhouse eustasy (e.g., Sames et al. 2016; Ray et al. 2019). A two-dimensional reconstruction of sedimentation rates in the study interval (Fig. 4), however, suggests that the regressive phases of TUR1 and TUR2 were accompanied by reduced sedimentation rates. Such a decoupling between shoreline movement and sedimentation rates appears incompatible with unforced progradation controlled by increasing sediment input. Instead, it is expected in sequences controlled by relative sea level change, i.e., change in accommodation, which restrains sediment accretion in the regressive tract. The sharp bases of TUR1 and TUR2 sandstones (Supplementary materials, Fig. S1 and S2) and apparent non-deposition or erosion beneath the prograding shoreface of TUR2 (Fig. 4) resemble scouring associated with relative sea-level fall and forced regression (cf. Plint 1988). Recently published numerical models (Willis et al. 2022), which simulate “normal” or unforced regression with static sea level (no background subsidence) suggest that relative sea-level fall is not a necessary prerequisite for the formation of sharp-based shoreface

deposits. Regressive tracts of sequences TUR1 and TUR2 could therefore represent transient stagnation in relative sea level rise. In any instance, considering active tectonic subsidence and positive background accommodation in the study interval (section 3.1; Supplementary Table S4), a mere deceleration in relative sea-level rise points to a short-term component in the sea-level forcing, thus arguing for sea-level-dominated rather than supply-dominated scenario.

Based on the above arguments, we posit that sequences TUR1 and TUR2 represent ~400-kyr fluctuations in relative sea level or the rate of relative sea-level rise. These changes might have originated from eustasy or local tectonics, the latter involving namely fault- or fold-related subsidence/uplift of parts of the depocenter due to compressional stress translated from the convergence of Iberia and Europe (Voigt et al. 2021). Detailed well-log correlations shown here and in previous studies (Uličný et al. 2009) suggest a relatively simple, wedge-shaped geometry of the lower Turonian basin fill with no distinct geometric or facies patterns that would suggest short-term intrabasinal faulting during the early Turonian. It is further considered unlikely that any crustal or mantle processes (e.g., review in Horton et al. 2018) would occur on time scales matching the 405-kyr astronomical period within a narrow uncertainty margin (section 3.1). The possible topographic, gravitational or rotational feedbacks to climate change (Horton et al. 2018; Mitrovica et al. 2020) would be strongly limited in their magnitude under greenhouse conditions. Other processes such as sediment loading (e.g., Lin et al. 2023) participated in creating the background accommodation, but their ability to produce astronomical-scale cycles in relative sea level requires systematic changes in sedimentation rates, which brings the argumentation back to the option of supply-dominated sequences that was rejected in the previous paragraph. Therefore, we conclude that eustatic (global) sea-level change provides the most consistent explanation for sequences TUR1 and TUR2. Supporting data can be sought in interbasinal correlation, although detailed sea-level records are scarce for the early Turonian highstand. For example, two sea-level cycles compatible with sequences TUR1 and TUR2 were inferred in the lower Turonian of U.S. Western Interior (Laurin and Sageman 2007, their sequences S5 and S6; see also Tibert et al. 2003). In addition, subaerial unconformities and relative sea-level fall coeval (within age uncertainty) with TUR2 have been interpreted from other European sites (e.g., Janetschke et al. 2015), Jordan platform (Wendler et al. 2014), and the

New Jersey margin (Miller et al. 2005). Additional comments on the possible forcing mechanisms can be found in Supplementary materials, Table S5.

3.3 Timing of eustatic sea-level change in the early Turonian

As argued in previous sections sequences TUR1 and TUR2 record relative sea-level change that originated from eustatic sea-level oscillations on the ~400-kyr time scale. Any stratigraphic record of eustasy is skewed non-linearly by the effects of subsidence, sediment input, depositional topography and sediment reworking, which prevent a full quantitative reconstruction of the original sea-level change. The shape of eustatic sea level cycle cannot be quantified in most instances. With a detailed time scale and high-resolution stratigraphy, however, it should be possible to constrain the depositional system to a level that allows a relatively precise estimation of the timing of eustatic sea-level maxima and minima. Here, we apply an empirical approach based on two-dimensional stratigraphic modeling (section 2.7). The model is constrained by the background accommodation (as defined in section 2.8) and sediment fluxes (estimated from the age-calibrated cross section; Fig. 3b). Other parameters such as wave-base depth and transport characteristics of the coarse and fine siliciclastic fractions are adjusted to reproduce the observed geometries (Fig. 3a). The primary input variable is eustatic sea-level change with a period of 405 kyr and amplitude ranging from 1 to 10 m. Several necessary assumptions must be made; due to uncertainties in quantitative data, eustatic sea-level oscillations are approximated by sinusoidal functions and siliciclastic sediment input is considered constant in the course of the ~400-kyr cycles. The model output is used here to calculate the phase offset between the key sequence stratigraphic surfaces and the sea-level forcing for a range of depositional scenarios constrained by the observed stratigraphy.

The maximum transgressive surfaces provide the most accurate tie points to eustasy as they are typically linked to the highest rate of relative sea-level rise (Mancini and Tew 1997; Galloway 1989; Supplementary Figure S3). The timing of inflection points in relative sea-level change, however, depends strongly on the shape of eustatic sea-level curve, which cannot be inferred from stratigraphic data. Hence, instead of referring to the inflection points, we quantify the timing of maximum transgressive surfaces and maximum regressive surfaces relative to the extremes of eustatic sea-level change. The results of numerical modeling (section 2.7; Supplementary Table S6 and Figure S6) suggest that, in the study

interval, the maximum transgression occurs 81 ±14 (2σ) kyr prior to the 405-kyr maximum in eustatic sea-level and maximum regression predates the 405-kyr minimum in eustatic sea-level by 65 ±22 (2σ) kyr. When combined with the correlation to 405-kyr metronome (Fig. 3), it is inferred that eustatic sea-level cycles were nearly ~180° out-of-phase relative to the 405-kyr eccentricity: eustatic minima postdate the 405-kyr eccentricity maxima by 60 kyr (±65 2σ), and eustatic maxima predate 405-kyr eccentricity minima by 11 (±54) to 67 (±67) kyr (Fig. 5; Tab. 1).

The results of numerical modeling further suggest that the non-linear response of nearshore stratigraphy to sea-level change contributes to the asymmetric proportion of transgressive vs. regressive intervals in sequences TUR1 and TUR2. The full scale of the observed asymmetry, however, cannot be explained by the depositional system itself, as the proportion of transgressive tracts in the simulated stratigraphy averages 46% (±5% 2σ), i.e., nearly twice as much as in the observed sequences. Most of the observed asymmetry was therefore likely inherited from the eustatic forcing.

3.4 Magnitude of eustatic sea-level change in the early Turonian

The absence of fluvial incision or detached shoreface deposits suggests that the rate of ~400-kyr eustatic falls never substantially exceeded the rate of background accommodation (158 ±17 m/Myr; section 3.1). Brief episodes when the short-term eustatic sea-level falls reached or marginally outpaced the rate of accommodation-space creation are, however, indicated by the sharp lower contacts of TUR1 and TUR2 sandstones (Supplementary materials, Figs. S1 and S2) and evidence for reduced sedimentation rates beneath the advancing shoreface (Fig. 4). Considering the ~400-kyr time scale and sinusoidal shape of eustatic sea-level change, the 158 (+17) m/Myr limit corresponds to an amplitude of c. 11 m (magnitude 22 m). This value can be considered a conservative upper limit for the short-term eustatic component. An attempt to refine this estimate with two-dimensional numerical modeling (section 2.7) suggests that eustatic magnitudes of 6 m or less are sufficient to explain the observed geometries and progradational distances (Supplementary Materials, Figure S7).

4. DISCUSSION

4.1 Phasing of eustatic sea-level change; icehouse vs. greenhouse regimes

Examples of sea-level cyclicity that can be linked accurately to eccentricity phasing are found in the icehouse regimes of the Cenozoic. The earliest Miocene, c. 18 to 22 Myr ago, exhibits a prominent 405-kyr pacing of oxygen isotope composition of benthic foraminifera, which has been attributed to ice-volume variations (Liebrand et al. 2017; for spectral estimates see Supplementary Materials, Figure S8). Correlation to astronomical solutions (Laskar et al. 2004, 2011) suggests that glacial retreat and glacioeustatic sea-level rise on the 400-kyr scale were coordinated with the rising phases of 405-kyr eccentricity (Figs. 6, 7). A similar phasing, although on the ~100-kyr eccentricity time scale is found in the Late Pleistocene (Fig. 7a), where deglaciations are driven by a combination of increased summer insolation at high-latitudes (e.g., Milankovitch 1941; Imbrie et al. 1992) and elevated CO_2 fluxes to the atmosphere (e.g., Ai et al. 2020). The Late Pleistocene deglaciations are relatively brief, and, in spite of an important role of axial obliquity in the causal mechanisms, phased with rising eccentricity (Fig. 7a). The distinct asymmetry of Late Pleistocene cycles (e.g., Hagelberg and Pisias 1991) is comparable to the asymmetry of ~400-kyr sea-level changes interpreted in the early Turonian (Figs. 5, 7). The timing of sea-level rise and fall relative to the ~400-kyr eccentricity phases is, however, incompatible with the icehouse examples (Figs. 6, 7), and suggests contrasting modes of continental water storage, different sensitivities to seasonal insolation, and possibly specific geography of the hydrological reservoirs.

4.2 Glaciation and glacioeustasy in the peak greenhouse

The question of inter-annual accumulation of ice at high latitudes and altitudes of the Cretaceous greenhouse has remained controversial for several decades, with compelling arguments on both sides of the discussion (e.g., Plint 1991; Miller et al. 2005; Bornemann et al. 2008; Flögel et al., 2011; Huber et al. 2018; Davies et al. 2020). Due to the limited access to near-field stratigraphic records of high latitudes, estimates of the rates and magnitudes of potential glacioeustasy must rely on sequence-stratigraphic interpretation of sea-level change and evaluation of isotopic proxies for temperature and ice volume. Considering the role of astronomical cycles in modulating summer insolation at high latitudes (e.g., Milankovitch 1941; Berger et al. 1993), the timing of sea-level change relative to the phase of astronomical parameters could provide additional clues.

The early Turonian data suggest that the maximum rates of eustatic sea-level fall postdated eccentricity minima (Figs. 5, 7c). This phasing essentially excludes the possibility of glacioeustasy on eccentricity time scales because the cryosphere expansion and buildup of ice volume would have to cope with increasing seasonality variation and rising magnitude of (precession-controlled) summer insolation extremes. This conflict is further highlighted by the proximity of the study interval to a ~2.4-Myr maximum in eccentricity modulation (Ma et al. 2019; Laurin et al. 2021), which must have resulted in enhanced summer insolation maxima (e.g., Berger et al. 1993). A similar argument can be made from the opposite perspective. In a glacioeustatic system, the highest rate of sea-level fall is expected at or immediately after the infection point of falling eccentricity (Figs. 6, 7a,b). The western depocenter of the Bohemian Cretaceous Basin became overfilled during deposition of sequences TUR1 through TUR3 (Fig. 3), which enhanced its sensitivity to relative sea-level falls or decelerations in relative sea-level rise. Under these conditions, even a minor eustatic fall would leave a stratigraphic record. Instead, however, the falling phase of 405-kyr eccentricity is associated with the opposite movement – transgression – in the study interval.

In summary, the results presented here argue against the possibility of substantial high-latitude and/or high-altitude glaciation during the peak greenhouse, in agreement with evidence for high temperatures in the Antarctic interior (e.g., Klages et al. 2020). It should be stressed, however, that the present study is limited to a relatively narrow interval of the peak early Turonian warmth. Potential glaciation episodes during colder phases of the mid-Cretaceous greenhouse are not disqualified by the above arguments.

4.3 Greenhouse sea-level control; reservoir characteristics

The data presented here constrain the time scales and phase of continental water storage responsible for sea-level oscillations during the early Turonian. The water transfers took place predominantly at the ~400-kyr eccentricity pace suggesting a role of seasonal insolation at a particular latitude or range of latitudes. As orbital eccentricity imparts its control on insolation primarily via amplitude modulation of precessional cycles (e.g., Hays et al. 1976, Berger et al., 1993), the prominence of eccentricity pacing may suggest a non-linear response of the climate system due to carbon-cycle feedback (e.g., Herbert 1997; Pälike et al. 2006; Laurin et al. 2017), or integration of seasonal insolation forcing across a

range of latitudes (Short et al. 1991; Zeebe et al. 2017). The latter option appears particularly favorable, because it offers an additive capacity of multiple hydrological reservoirs across continental regions, thus partly eliminating the issue of limited capacity of continental reservoirs (cf. Davies et al. 2020). An intervening role of the carbon cycle via changes in the concentration of greenhouse gases can be considered as a possible source of the asymmetry of sea-level response to insolation (cf. Pälike et al. 2006).

The most efficient alternative to glacioeustasy is a storage of water in aquifers and lakes, i.e., aquifer- and limno-eustasy (Hay and Leslie 1990; Jacobs and Sahagian 1993; Wagreich et al. 2014; Wendler et al. 2016). However, assuming the ocean area of 373 $x10^6$ km^2 (Davies et al. 2020), the 6-m limit would be equivalent to 2.2 $x10^6$ km^3 of water, comparable to 10 % of the total groundwater stored in the uppermost 2 km of the present-day continental crust (cf. Gleeson et al. 2016). Such volumes challenge even the most optimistic estimates of the maximum capacity of active continental reservoirs (Davies et al. 2020), and so the rates and capacities of this mechanism remain a major issue that could be addressed by future modeling efforts. In any instance, the search for water storage responsible for greenhouse sea-level change should focus on reservoirs that can charge (expand) with rising eccentricity and discharge (decay) with declining eccentricity on the 405-kyr time scale. The eccentricity-dominated structure of sea-level change does not provide many clues on the geographic location of the continental reservoirs, but the absence of distinct obliquity component suggests no or limited sensitivity to integrated summer insolation of high latitudes (e.g., discussion in Huybers and Tziperman 2008). Considering the abundance of eccentricity-paced monsoonal records in the mid-Cretaceous (e.g., Mitchell et al. 2008; Sprovieri et al. 2013), changes in precipitation/evaporation balance at low to middle latitudes of Africa, Asia and South America could provide the desired climate forcing.

Thermal contraction and expansion of seawater (steric effects) in response to changing insolation likely participated as a proportionally relevant component of the greenhouse eustasy, although the time scales, phases and magnitudes remain uncertain. Assuming the average expansion coefficient of 2.0-2.5 $x10^{-4}$ K^{-1}, the estimated maximum oscillation in sea level (6 m) would require a change in the average temperature of the entire ocean by 6-8 °C. Such a change appears unfounded, but smaller (~2 m) contributions related to changes in the rate of intermediate and deep water formation are plausible

(Schulz and Schäfer-Neth 1997). Depending on the particular oceanographic conditions, the steric effects might have enhanced certain phases of aquifer-eustatic change and acted as a factor in transferring variance from precessional insolation cycles to the excentricity time scales.

The anti-phased relationship of early Turonian sea-level change and glacioeustasy (Figs. 6, 7) appears to support the concept of destructive interference of aquifer eustasy and glacioeustasy upon greenhouse-icehouse transitions proposed by Ray et al. (2019). It should be noted, however, that eccentricity scale glacioeustasy, examples of which are given in this paper, is probably limited to mature, stabilized icehouse regimes. Both empirical and theoretical data suggest that early transitional phases towards an icehouse regime would likely experience ice-volume variability at the obliquity frequencies (e.g., Hyubers 2006; Langebroek et al. 2009). Thus, both additive and subtractive combinations of aquifer and glacial storage appear possible during the transitional phases.

5. SUMMARY

Transgressive-regressive changes recorded in the early Turonian segment of the Cretaceous thermal maximum (~93-94 Myr ago) suggest a pattern of small-scale (≤6 m) sea-level oscillations following the 405-kyr cycle of orbital eccentricity. A high-resolution astronomical framework covering two complete 405-kyr cycles suggests a distinct asymmetry of eustatic sea-level change, with brief episodes of rising sea level superimposed upon the falling phase of 405-kyr eccentricity and protracted sea-level falls covering the minimum, rise and maximum of the 405-kyr eccentricity cycle. Sea-level minima postdate the 405-kyr eccentricity maxima by 60 kyr (±65 2σ), and sea-level maxima predate 405-kyr eccentricity minima by 11 (±54) to 67 (±67) kyr. This phasing contrasts markedly with the phasing of eccentricity-controlled glacioeustatic sea-level fluctuations of icehouse regimes suggesting major differences in the location and insolation sensitivity of key hydrological reservoirs under icehouse and greenhouse climates. The continental water storage responsible for greenhouse eustasy expanded preferably upon increasing eccentricity and rising amplitude of precession-paced seasonality variations on the 405-kyr time scale. The stored water volume decreased upon decline in the 405-kyr seasonality cycle. These relationships point to a possible control via precipitation/evaporation balance at low and middle latitudes and

make it possible to further evaluate the existing hypotheses on aquifer-, limno- and steric eustasy under greenhouse climates. The phasing of astronomically paced sea-level change can help to delineate the threshold for high-latitude ice buildup upon greenhouse-icehouse transitions.

ACKNOWLEDGMENTS

This research was supported by the Czech Science Foundation (GAČR) project No. 17-10982S and research program RVO 67985530 of the Czech Academy of Sciences. Acquisition of digital well-log data and core samples was made possible through cooperation with DIAMO, s.p. and the Czech Geological Survey. Petr Kolář kindly provided valuable comments on quantification of data uncertainty. Comments by two anonymous reviewers helped considerably to improve the first version of this manuscript.

DATA AVAILABILITY

Data used in this paper are included in the Supplementary Materials. The code for ShamFlu2D is available upon request.

REFERENCES

Ai, X.E., Studer, A.S., Sigman, D.M., Martínez-García, A., Fripiat, F., Thöle, L.M., Michel, E., Gottschalk, J., Arnold, L., Moretti, S., Schmitt, M., Oleynik, S., Jaccard, S.L., Haug, G.H., 2020, Southern Ocean upwelling, Earth's obliquity, and glacial-interglacial atmospheric CO2 change. Science 370, 1348–1352.

Allen, P. A., & Allen, J. R., 2013, Basin analysis: Principles and application to petroleum play assessment. John Wiley & Sons.

Berger, A., Loutre, M.F., and Laskar, J., 1992, Stability of the astronomical frequencies over the Earth's history for paleoclimate studies: Science, v. 255, p. 560–566.

Berger A, Loutre M-F, and Tricot C. 1993. Insolation and Earth's orbital periods. J. Geophys. Res. 98 (D6), 10341–62

Bornemann, A., Norris, R.D., Friedrich, O., Beckmann, B., Schouten, S., Damste, J.S.S., Vogel, J., Hofmann, P., Wagner, T., 2008. Isotopic evidence for glaciation during the Cretaceous supergreenhouse. Science 319, 189–192.

Boylan, A, Waltham, D, Bosence, D, Badenas, B and Aurell, M., 2002. Digital rocks: linking forward modeling to carbonate facies. Basin Research 14, 401-415

Davies, A., Gréselle, B., Hunter, S.J., Baines, G., Robson, C., Haywood, A.M., Ray, D.C., Simmons, M.D., van Buchem, F.S.P., 2020, Assessing the impact of aquifer-eustasy on short-term Cretaceous sea-level, Cretaceous Research, 112, 104445.

Flögel, S., Wallmann, K., Kuhnt, W., 2011. Cool episodes in the Cretaceous – exploring the effects of physical forcings on Antarctic snow accumulation. Earth Planet. Sci. Lett. 307, 279–288.

Friedrich, O., Norris, R. D., Erbacher, J. (2012). Evolution of middle to Late Cretaceous oceans - A 55 m.y. record of Earth's temperature and carbon cycle. Geology 40, 107–110.

Galloway, W.E., 1989, Genetic stratigraphic sequences in basin analysis I: architecture and genesis of flooding-surface bounded depositional units: American Association of Petroleum Geologists, Bulletin, v. 73, p. 125–142.

Gleeson, T., Befus, K.M., Jasechko, S., Luijendijk, E., and Cardenas, M.B., 2016, The global volume and distribution of modern groundwater. Nature Geoscience, 9, 161–167.

Gradstein, F. M., Ogg, J. G., Schmitz, M. D., and Ogg, G. M., 2020, The geologic time scale 2020. Boston, MA, Elsevier, 1390 pp.

Hagelberg, T., and Pisias, N., 1991, Linear and nonlinear couplings between orbital forcing and the marine $\delta^{18}O$ record during the Late Neogene. Paleoceanography, 6, 729-746.

Hancock, J. M. and E. G. Kauffman, 1979, The great transgressions of the Late Cretaceous. Journal of the Geological Society 136, 175 - 186.

Hay, W.W., Leslie, M.A., 1990. Sea Level Change: Studies in Geophysics. National Academy of Sciences, Washington (161-170 p).

Hay, W. W., DeConto, R. M., Wold, C. N., Wilson, K. M., Voigt, S., Schulz, M., et al., 1999, Alternative global Cretaceous paleogeography. In E. Barrera, & C. C. Johnson (Eds.), Evolution of the cretaceous ocean-climate system, Geological Society of America Special Paper 332 (pp. 1–47). Boulder, CO: Geological Society of America.

Hays, J. D., Imbrie, J. and Shackleton, N. J., 1976, Variations in the Earth's orbit: Pacemaker of the ice ages, Science, 194, 1121–1132.

Herbert, T. D., 1997, A long marine history of carbon cycle modulation by orbital-climatic changes. Proceedings of the National Academy of Sciences of the United States of America, 94(16), 8362–8369. https://doi.org/10.1073/pnas.94.16.8362

Horton, B. P., Kopp, R. E., Garner, A. J., Hay, C. C., Khan, N. S., Roy, K., Shaw, T. A., 2018, Mapping Sea-Level Change in Time, Space, and Probability. Annual Review of Environment and Resources, 43, 481-521. https://doi.org/10.1146/annurev-environ- 102017- 025826

Huber, B. T., MacLeod, K. G., Watkins, D. K. & Coffin, M. F., 2018, The rise and fall of the Cretaceous Hot Greenhouse climate. Glob. Planet. Change 167, 1–23.

Huybers, P. J. 2006. Early Pleistocene glacial cycles and the integrated summer insolation forcing. Science 313 (5786), 508-511.

Huybers, P., and E. Tziperman, 2008, Integrated summer insolation forcing and 40,000-year glacial cycles: The perspective from an ice-sheet/energy-balance model, Paleoceanography, 23, PA1208, doi:10.1029/2007PA001463.

Imbrie, J., Boyle, E.A., Clemens, S., Duffy, A., Howard, W., et al., 1992, On the structure and origin of major glaciation cycles: 1. Linear responses to Milankovitch forcing. Paleoceanography 7, 701–38.

Jacobs, D.K., Sahagian, D.L., 1993. Climate-induced fluctuations in sea level during non-glacial times. Nature 361 (6414), 710–712.

Janetschke, N., Niebuhr, B., Wilmsen, M., 2015, Interregional sequence-stratigraphical synthesis of the Plänerkalk, Elbtal and Danubian Cretaceous groups (Germany):

Cenomanian–Turonian correlations around the Mid-European Island, Cretaceous Research, 56, 530-549.
Klages, J. P. et al., 2020, Temperate rainforests near the South Pole during peak Cretaceous warmth. Nature 580, 81–86.
Langebroek, P. M., Paul, A., and Schulz, M., 2009, Antarctic ice-sheet response to atmospheric CO_2 and insolation in the Middle Miocene, Clim. Past, 5, 633-646, doi:10.5194/cp-5-633-2009.
Langebroek, P. M., A. Paul, and M. Schulz, 2010, Simulating the sea level imprint on marine oxygen isotope records during the middle Miocene using an ice sheet–climate model, Paleoceanography, 25, PA4203, doi:10.1029/2008PA001704.
Laskar, J., 2020, Astrochronology. In F. M. Gradstein, J. G. Ogg, M. D. Schmitz, & G. M. Ogg (Eds.), The geologic time scale 2020 (pp. 139–158). Boston, MA: Elsevier. https://doi.org/10.1016/B978-0-12-824360-2.00004-8
Laskar, J., Fienga, A., Gastineau, M., & Manche, H., 2011, La2010: A new orbital solution for the long-term motion of the Earth. Astronomy and Astrophysics, 532, A89. https://doi.org/10.1051/0004-6361/201116836
Laskar, J., Robutel, P., Joutel, F., Gastineau, M., Correia, A. C. M., & Levrard, B., 2004, A long-term numerical solution for the insolation quantities of the Earth. Astronomy and Astrophysics, 428, 261–285. https://doi.org/10.1051/0004-6361:20041335
Laurin, J., Sageman, B.B., 2007, Cenomanian-Turonian coastal record in SW Utah, USA: Orbital-scale transgressive-regressive events during oceanic anoxic event II. J. Sediment. Res. 77 (9–10), 731–756.
Laurin, J., Meyers, S.R., Uličný, D., Jarvis, I., Sageman, B.B., 2015, Axial obliquity control on the greenhouse carbon budget through middle- to high-latitude reservoirs. Paleoceanography 30, 133–149. https://doi.org/10.1002/ 2014PA002736.
Laurin, J., Růžek, B., Giorgioni, M., 2017. Orbital signals in carbon isotopes: phase distortion as a signature of the carbon cycle. Paleoceanography 32, 1236–1255. https://doi.org/10.1002/2017PA003143.
Laurin, J., Uličný, D., Čech, S., Trubač, J., Zachariáš, J., & Svobodová, A., 2021, Chronology and eccentricity phasing for the Early Turonian greenhouse (∼93–94 Ma): Constraints on astronomical control of the carbon cycle. Paleoceanography and Paleoclimatology, 36, e2020PA004188.
Liebrand, D., Beddow, H. M., Lourens, L. J., Pälike, H., Raffi, I., Bohaty, S. M., Hilgen, F. J., Saes, M. J. M. M., Wilson, P. A., van Dijk, A. E., Hodell, D. A., Kroon, D., Huck, C. E., Batenburg, S. J., Dijk, A. E. Van, Hodell, D. A., Kroon, D., Huck, C. E. and Batenburg, S. J., 2016, Cyclostratigraphy and eccentricity tuning of the early Oligocene through early Miocene (30.1–17.1 Ma): *Cibicides mundulus* stable oxygen and carbon isotope records from Walvis Ridge Site 1264, Earth Planet. Sci. Lett. 450, 392–405, doi:10.1016/j.epsl.2016.06.007
Liebrand, D., de Bakker, A. T. M., Beddow, H. M., Wilson, P. A., Bohaty, S. M., Ruessink, G., Pälike, H., Batenburg, S. J., Hilgen, F. J., Hodell, D. A., Huck, C. E., Kroon, D., Raffi, I., Saes, M. J. M., van Dijk, A. E. and Lourens, L. J., 2017, Evolution of the early Antarctic ice ages, Proc. Natl. Acad. Sci., 114(15), 3867–3872, doi:10.1073/pnas.1615440114
Lin, Y., Whitehouse, P. L., Hibbert, F. D., Woodroffe, S. A., Hinestrosa, G., and Webster, J. M., 2023, Relative sea level response to mixed carbonate-siliciclastic sediment loading along the Great Barrier Reef margin. Earth and Planetary Science Letters, 607, 118066. https://doi.org/10.1016/j.epsl.2023.118066

Ma, C., Meyers, S. R., & Sageman, B. B., 2019, Testing Late Cretaceous astronomical solutions in a 15 million year astrochronologic record from North America. Earth and Planetary Science Letters, 513, 1–11. https://doi.org/10.1016/j.epsl.2019.01.053

Mancini, E.A., and Tew, B.H., 1997, Recognition of maximum flooding events in mixed siliciclastic-carbonate systems: key to global chronostratigraphic correlation: Geology, v. 25, p. 351-354.

Milankovitch, M., 1941. Kanon der Erdbestrahlung und seine andwendung auf das eiszeitenproblem. In: Royal Serbian Academy Special Publication 132, vol. 33. Königlich Serbische Akademie, Belgrade.

Miller, K.G., Wright, J.D., Browning, J.V., 2005. Visions of ice sheets in a greenhouse world. Mar. Geol. 217, 215–231.

Mitchell, R.N., Bice, D.M., Montanari, A., Cleaveland, L.C., Christianson, K.T., Coccioni, R., Hinnov, A.L., 2008. Oceanic anoxic cycles? Orbital prelude to the Bonarelli Level (OAE 2). Earth Planet. Sci. Lett. 26, 1–16.

Mitchell, A., Uličný, D., Hampson, G.J., Allison, P.A., Gorman, G.J., Piggott, M.D., Wells, M.R., Pain, C.C., 2010. Modelling tidal current-induced bed shear stress and palaeocirculation in an epicontinental seaway: the Bohemian Cretaceous Basin, Central Europe. Sedimentology 57, 359–388. http://dx.doi.org/10.1111/j.1365-3091.2009.01082.x.

Mitrovica, J. X. Austermann, J., Coulson, S., Creveling, J. R., Hoggard, M. J., Jarvis, G. T., and Richards, F. D., 2020, Dynamic Topography and Ice Age Paleoclimate. Annual Review of Earth and Planetary Sciences, 48, 585-621. https://doi.org/10.1146/annurev-earth-082517- 010225

Pagani, M., Huber, M., Sageman, B., 2014, Greenhouse Climates, In (Eds.): Heinrich D. Holland, Karl K. Turekian, Treatise on Geochemistry (Second Edition), Elsevier, 281-304.

Pälike, H., Norris, R.D., Herrle, J.O., Wilson, P.A., Coxall, H.K., Lear, C.H., Shackleton, N.J., Tripati, A.K., Wade, B.S., 2006. The heartbeat of the Oligocene climate system. Science 314, 1894–1898. http://dx.doi.org/10.1126/science.1133822.

Plint, A.G., 1991. High-frequency relative sea-level oscillations in the Upper Cretaceous shelf clastics of the Alberta foreland basin: possible evidence for a glacio-eustatic control. In: McDonald, D.I.M. (Ed.), Sedimentation, Tectonics and Eustasy. Internat. Assoc. Sedimentol. Spec. Publ, 12, pp. 409–428.

Plint, A.G., 1988. Sharp-based shoreface sequences and “offshore bars” in the Cardium Formation: their relationship to relative changes in sea level. In: Wilgus, C.K., Hastings, B.S., Posamentier, H.W., van Wagoner Ross, C.A., Kendall, C.G.St.C. (Eds.), Sea Level Changes: An Integrated. In: Approach. Soc. Econ. Paleontol. Miner., Spec. Pub., vol. 42, pp. 357–370.

Plint, A.G., Uličný, D., Čech, S., Walaszczyk, I., Gröcke, D.R., Laurin, J., Shank, J.A., Jarvis, I., 2022, Trans-Atlantic correlation of Late Cretaceous high-frequency sea-level cycles, Earth and Planetary Science Letters, 578, 117323.

Ray, D.C., van Buchem, F.S.P., Baines, G., Davies, A., Gréselle, B., Simmons, M.D., Robson, B., 2019. The magnitude and cause of short-term eustatic Cretaceous sea- level change: a synthesis. Earth-Sci. Rev. 197, 102901. https://doi.org/10.1016/j. earscirev.2019.102901.

Sames, B., Wagreich, M., Wendler, J.E., Haq, B.U., Conrad, C.P., Melinte-Dobrinescu, M.C., Hu, X., Wendler, I., Wolfgring, E., Yilmaz, I.Ö., Zorina, S.O., 2016. Review: short-term

sea-level changes in a greenhouse world - a view from the Cretaceous. Palaeogeogr. Palaeoclimatol. Palaeoecol. 441, 393–411.
Schulz, M. and Schäfer-Neth, C., 1997, Translating Milankovitch climate forcing into eustatic sea-level fluctuations via warm saline deep waters: a conceptual link, Terra nova, 9, 228-231.
Short, D. A., Mengel, J. G., Crowley, T. J., Hyde, W. T., & North, G. R., 1991, Filtering of Milankovitch cycles by Earth's geography. Quaternary Research, 35(02), 157–173. https://doi.org/10.1016/0033-5894(91)90064-C
Spratt, R. M. and Lisiecki, L. E., 2016, A Late Pleistocene sea level stack, Clim. Past, 12, 1079–1092, https://doi.org/10.5194/cp-12-1079-2016.
Sprovieri, M., Sabatino, N., Pelosi, N., Batenburg, S. J., Coccioni, R., Iavarone, M., & Mazzola, S., 2013, Late Cretaceous orbitally-paced carbon isotope stratigraphy from the Bottaccione Gorge (Italy). Palaeogeography Palaeoclimatology Palaeoecology, 379-380, 81–94. https://doi. org/10.1016/j.palaeo.2013.04.006
Thorne, J.A., and Swift, D.J.P., 1991, Sedimentation on continental margins, VI: a regime model for depositional sequences, their component systems tracts, and bounding surfaces, in Swift, D.J.P., Oertel, G.F., Tillman, R.W., and Thorne, J.A., eds., Shelf Sand and Sandstone Bodies: International Association of Sedimentologists, Special Publication 14, p. 189–255.
Tibert, N.E., Leckie, R.M., Eaton, J.G., Kirkland, J.I., Colin, J.P., Leithold, E.L., McCormic, M., 2003, Recognition of relative sea level change in Upper Cretaceous coal-bearing strata: a paleoecological approach using agglutined foraminifera and ostracodes to detect key stratigraphic surfaces. In: Olson, H., Leckie, R.M. (Eds.), Microfossils as a Proxy for Sea Level Changes and Stratigraphic Discontinuities. Society for Sedimentary Geology (SEPM) Special Publication, pp. 263–299.
Uličný, D., Laurin, J., Čech, S., 2009. Controls on clastic sequence geometries in a shallow-marine, transtensional basin: the Bohemian Cretaceous Basin, Czech Republic. Sedimentology 56, 1077–1114.
Uličný, D., Jarvis, I., Gröcke, D. R., Čech, S., Laurin, J., Olde, K., et al., 2014, A high-resolution carbon-isotope record of the Turonian stage correlated to a siliciclastic basin fill: Implications for mid-Cretaceous sea-level change. Palaeogeography, Palaeoclimatology, Pal- aeoecology, 405, 42–58.
Van Wagoner, J.C., Posamentier, H.W., Mitchum, R.M., Vail, P.R., Sarg, J.F., Loutit, T.S., and Hardenbol, J., 1988, An overview of fundamentals of sequence stratigraphy and key definitions, in Wilgus, C.K., Hastings, B.S., Kendall, C.G.St.C., Posamentier, H.W., Ross, C.A., and Van Wagoner, J.C., eds., Sea-Level Changes: An Integrated Approach: SEPM, Special Publication 42, p. 39–44.
Voigt, T., Kley, J., and Voigt, S., 2021, Dawn and dusk of Late Cretaceous basin inversion in central Europe. Solid Earth. 12, 1443–1471. https://doi.org/10.5194/se-12-1443-2021
Wagreich, M., Lein, R., Sames, B., 2014. Eustasy, its controlling factors, and the limno-eustatic hypothesis – concepts inspired by Eduard Suess. Austrian J, Earth Sci. 107 (1), 115–131.
Waltham, D., 2015, Milankovitch period uncertainties and their impact on cyclostratigraphy. Journal of Sedimentary Research, 85, 990– 998. https://doi.org/10.2110/jsr.2015.66

Wendler, J. E., Meyers, S. R., Wendler, I., & Kuss, J., 2014, A million-year-scale astronomical control on Late Cretaceous sea-level. Newsletters on Stratigraphy, 47, 1–19. https://doi.org/10.1127/0078-0421/2014/0038

Wendler, J.E., Wendler, I., Vogt, C., Kuss, J., 2016. Link between cyclic eustatic sea-level change and continental weathering: evidence for aquifer-eustasy in the Cretaceous. Palaeogeogr. Palaeoclimatol. Palaeoecol. 441 (3), 430–437.

Willis, B.J., Sun, T. & Ainsworth, R.B., 2022, Sharp-based shoreface successions reconsidered in three-dimensions: A forward stratigraphic modelling perspective. The Depositional Record, 8, 685– 717. https://doi.org/10.1002/dep2.177

Zachos, J., Pagani, M., Sloan, L., Thomas, E., Billups, K., 2001, Trends, rhythms, and aberrations in global climate 65 Ma to present. Science 292, 686-93.

Zeebe, R. E., & Lourens, L. J., 2019, Solar System chaos and the Paleocene-Eocene boundary age constrained by geology and astronomy. Science, 365(6456), 926–929. https://doi.org/10.1126/science.aax0612

Zeebe, R. E., Westerhold, T., Littler, K., & Zachos, J. C., 2017, Orbital forcing of the Paleocene and Eocene carbon cycle. Paleoceanography, 32, 440–465. https://doi.org/10.1002/2016PA003054

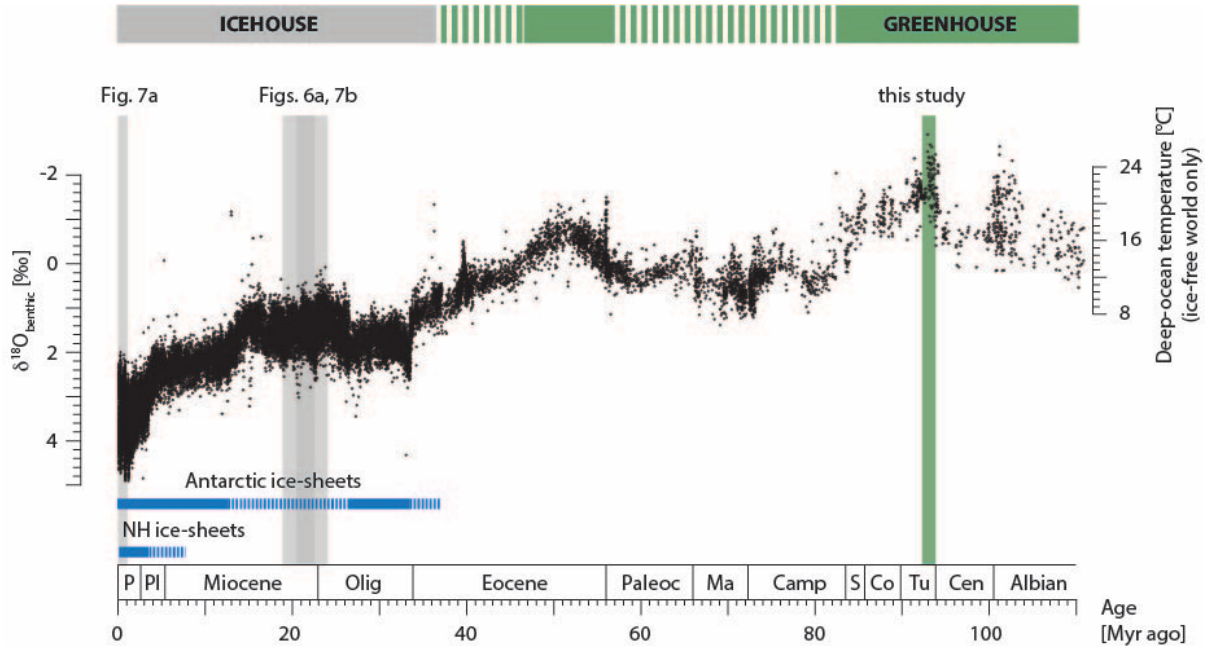

Figure 1. Temperature evolution of the last 110 Myr. Oxygen-isotope composition of benthic foraminifera ($\delta^{18}O_{benthic}$) and estimated temperature after Friedrich et al. (2012); chronostratigraphic boundaries have been updated based on GTS2020 (Gradstein et al. 2020). High-latitude glaciation is indicated by blue bars (dashed = ephemeral; Zachos et al. 2001). Abbreviations: P = Pleistocene, Pl = Pliocene, Olig = Oligocene, Paleoc = Paleocene, Ma = Maastrichtian, Camp = Campanian, S = Santonian, Co = Coniacian, Tu = Turonian, Cen = Cenomanian.

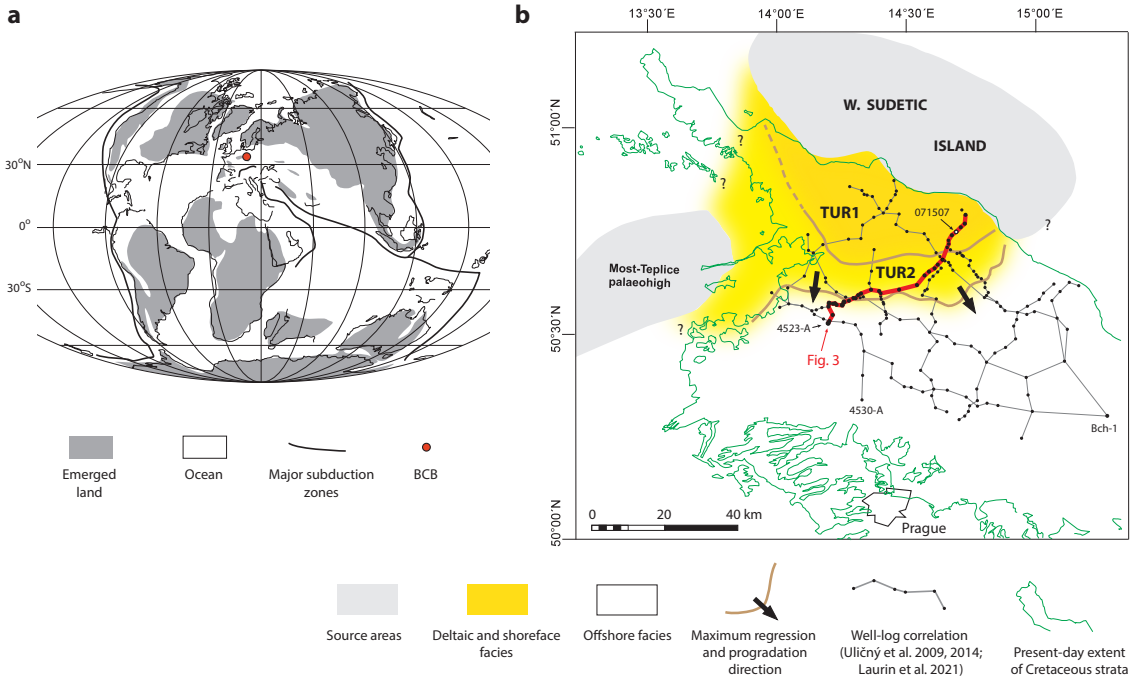

Figure 2. Paleogeographic context. **(a)** Plate tectonic reconstruction after Hay et al. (1999). Land/sea distribution is simplified after the PALEOMAP Project, C.R. Scotese (www.scotese.com). BCB = the Bohemian Cretaceous Basin. **(b)** Detail of the study area (modified after Uličný et al. 2009, 2014) plotted in the present-day coordinate system.

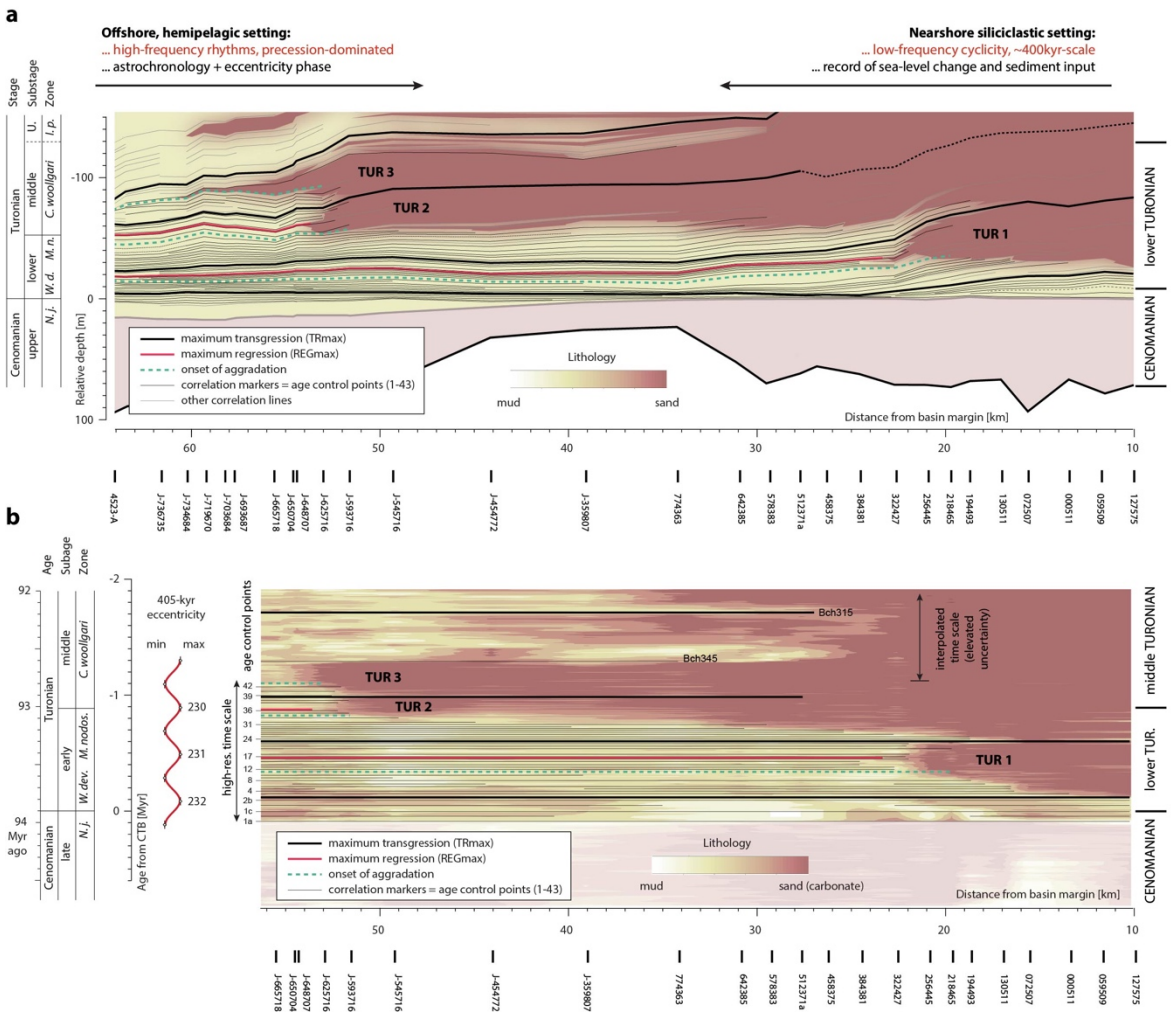

Figure 3. Cross-section of the study interval illustrating the sources of astronomical framework and sea-level record; lower to middle Turonian, western part of the Bohemian Cretaceous Basin (Fig. 2). **(a)** Cross-section plotted in the depth domain. Lithology is based on manual, semi-quantitative ranking of gamma-ray logs; brown color denotes the shoreface envelope. Labels at the bottom identify boreholes used in the correlation panel; full version is included in the Supplementary materials, Figure S1. **(b)** The same cross-section restored in the time domain. Lithology is based on numerical ranking of normalized gamma-ray logs, and presented as the proportion of sand-dominated shoreface siliciclastics; isolated brown streaks in the offshore setting are attributed to hemipelagic limestones (which are similar in their gamma-ray signature to coarse-grained siliciclastics). High-resolution chronology after Laurin et al. (2021); age control points are denoted by black lines; numbering (1-43) as in Supplementary Figure S1 and Table S1; Bch315 and Bch345 are interpolated ages (Supplementary Table S2). Correlation to the 405-kyr eccentricity metronome (Laskar 2020) is indicated along with the uncertainty of its phase relative to the local stratigraphy (vertical bars = 2σ); uncertainty relative to the formal chronostratigraphic framework (the Cenomanian/Turonian boundary; CTB) is ±80 kyr (not shown; Laurin et al. 2021). Abbreviations: *N. j.* = *Neocardioceras juddii*, *W. dev.* = *Watinoceras devonense*, *M. nodos.* = *Mammites nodosoides*, *C. woollgari* = *Collignoniceras woollgari*.

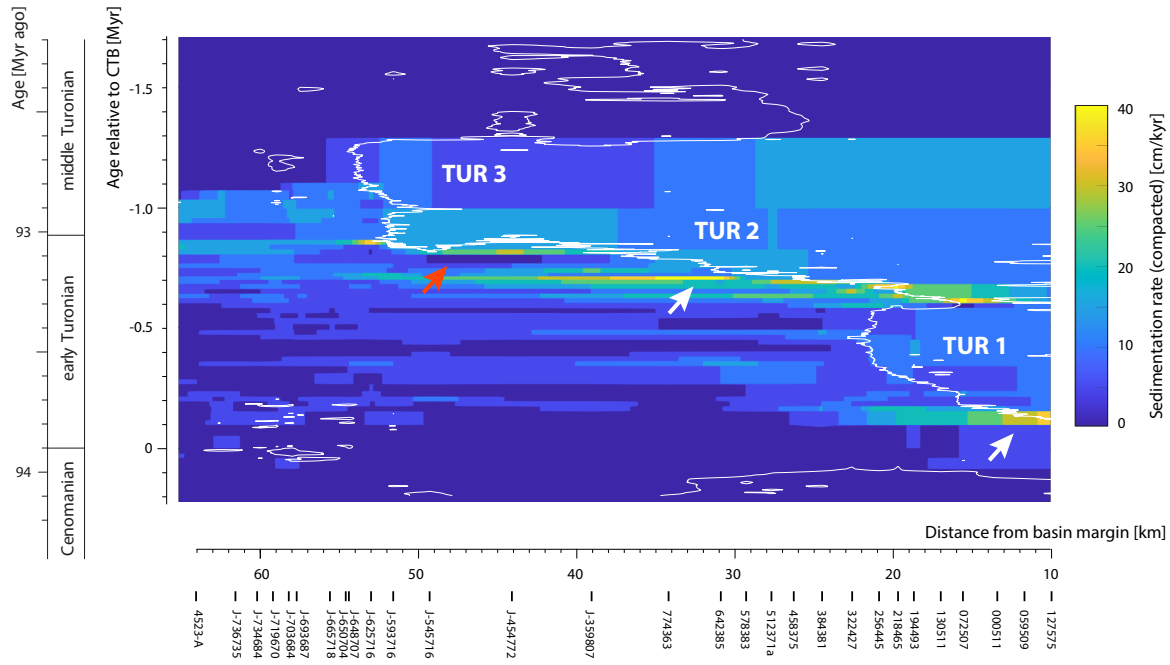

Figure 4. Two-dimensional reconstruction of compacted sedimentation rates; based on age-calibrated cross-section, Figure 3b. Shoreface siliciclastics are outlined by a white curve (30% sand in normalized gamma-ray logs). Note increased accumulation rates during the early phases of TUR1 and TUR2 regressions (white arrows). Red arrow points to an interval of non-deposition and possible scouring in front of the advancing shoreface (cf. forced regression of Plint 1988).

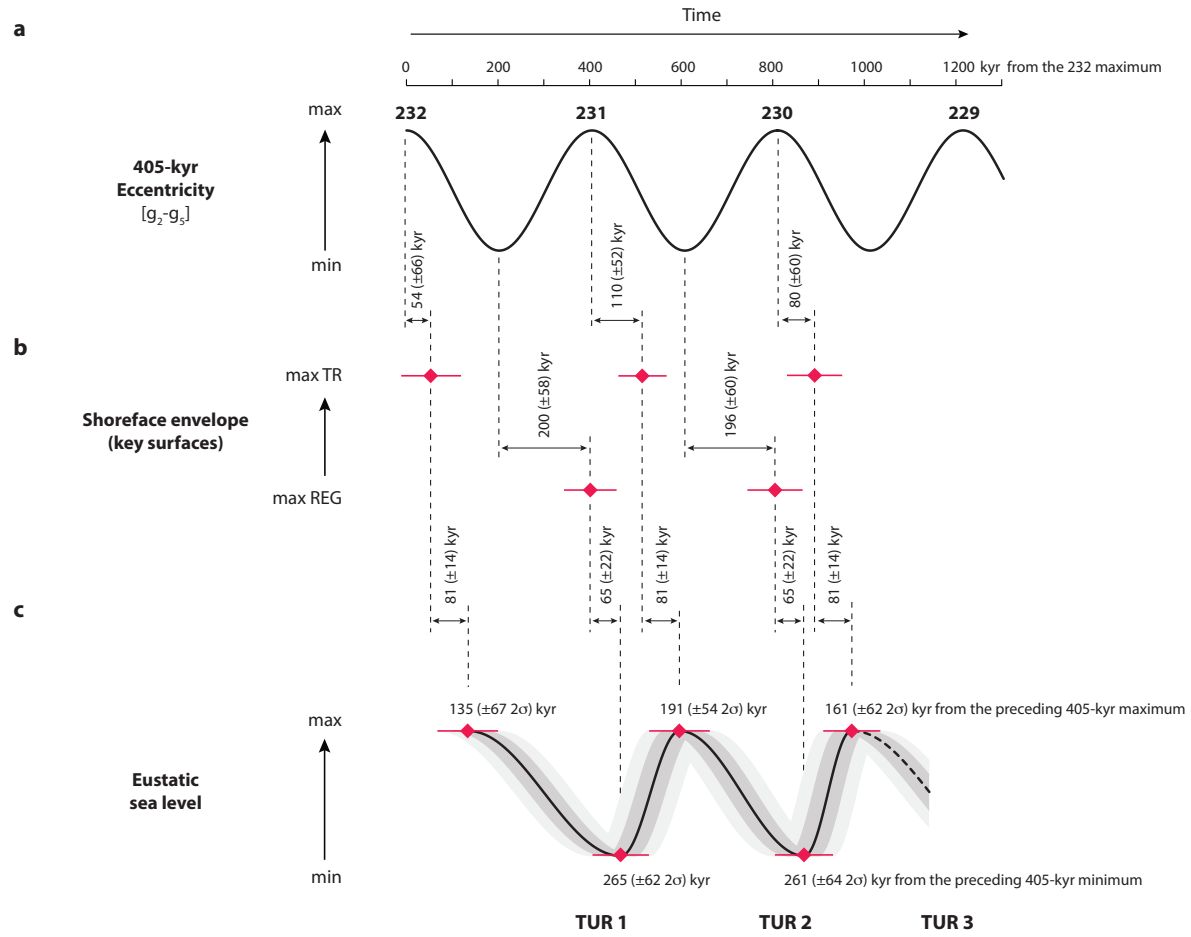

Figure 5. Reconstruction of the phasing of ~400-kyr eustatic sea-level change; early to middle Turonian. **(a)** 405-kyr eccentricity metronome (Laskar 2020). **(b)** Surfaces of maximum transgression (max TR) and maximum regression (max REG) of sequences TUR1 and TUR2 are tied to the astronomical time scale and phase of 405-kyr eccentricity (Fig. 3; Supplementary materials, Figs. S1 and S2; additional details in Laurin et al. 2021). **(c)** Inferred phasing of eustatic maxima and minima. Sensitivity tests with a two-dimensional numerical model (section 2.7) are used to estimate the degree of phase distortion inherent in the depositional system, and quantify the phase differences between transgressive-regressive surfaces and the extremes in eustatic sea-level change. A sinusoidal interpolation is applied between sea-level maxima and minima. Note that the main focus of this reconstruction is the phasing (horizontal axis); the vertical dimension (magnitude) of inferred eustatic cycles is arbitrary and no attempt is made to scale the magnitudes proportionally to transgressive-regressive changes. Grey shading denotes 1σ and 2σ uncertainties.

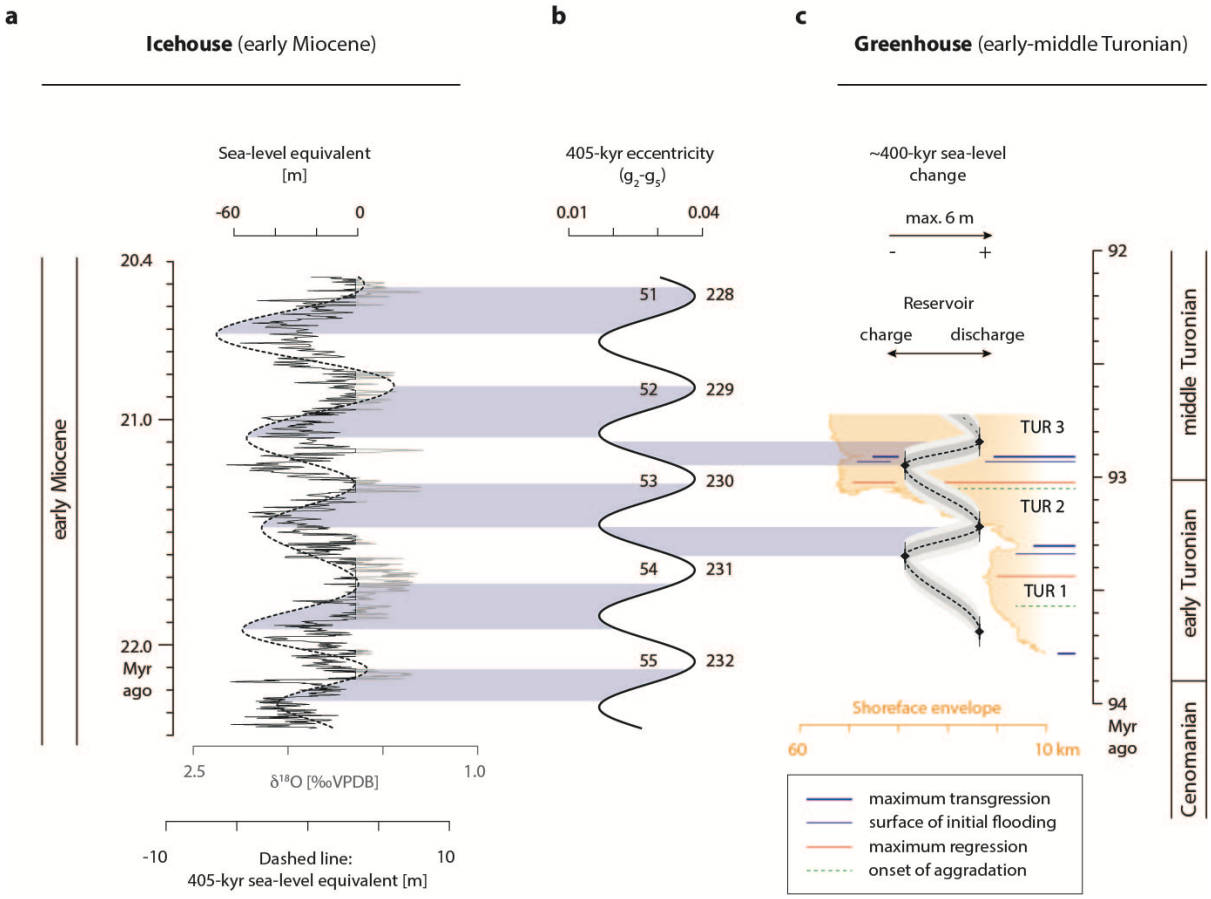

Figure 6. Comparison of the 405-kyr cyclicity in sea-level change between icehouse and greenhouse scenarios. **(a)** Example of 400-kyr paced icehouse record, early Miocene (Liebrand et al. 2017). Oxygen-isotope composition of benthic foraminifera (*Cibicides mundulus*) from ODP Site 1264 (δ^{18}O; Liebrand et al. 2016) serve as a proxy for temperature and ice-volume variations; values ≥1.65 ‰ VPDB are considered proportional to ice volume (see discussion in Liebrand et al. 2017); glacioeustatic sea-level equivalent is calculated assuming 0.1‰ enrichment in δ^{18}O per 10 m of sea-level change (Langebroek et al. 2010). Dashed line = filtered 405-kyr component of the sea-level equivalent; Taner filter, 2.47 ±1.00 cycle/Myr; see also Supplementary materials, Fig. S8. **(b)** The 405-kyr eccentricity metronome (Laskar 2020); numbers to the left and right of eccentricity maxima refer to the order of 405-kyr cycles relative to the present day (early Miocene to the left and early Turonian to the right). **(c)** The early-middle Turonian greenhouse (this study). Ochre shading denotes the shoreface envelope (30% sand in normalized gamma-ray logs; Fig. 3). The rising arms of sea-level cycles are highlighted by blue shading in both the Miocene and Turonian examples. Note the differences in phasing relative to the 405-kyr metronome.

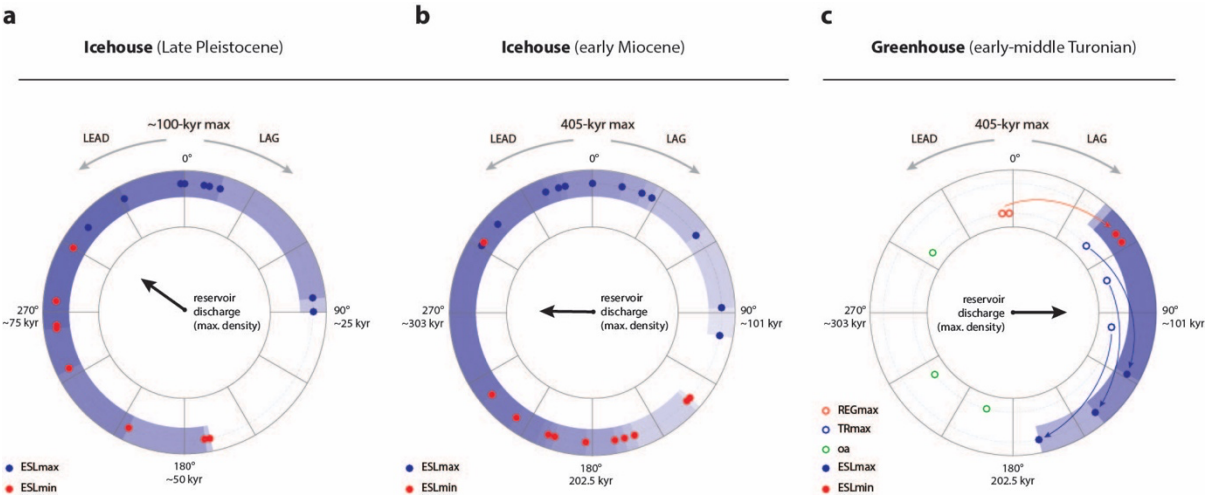

Figure 7. The phasing of eustatic sea-level change relative to the eccentricity forcing. Sea-level maxima (ESLmax) and minima (ESLmin) are marked by blue dots and red dots, respectively. Blue shading highlights the rising phases of sea-level cycles, i.e., reservoir discharge or decay; depth of the color is proportional to the number of observations. **(a)** Late Pleistocene icehouse, 0-800 kyr ago (Spratt and Lisiecki 2016), plotted against the short-eccentricity (~100-kyr) phase. **(b)** latest Oligocene to early Miocene icehouse, 19-24 Myr ago (Liebrand et al. 2017), plotted against the long-eccentricity (405-kyr) phase. **(c)** early Turonian greenhouse, ~93-94 Myr ago (this study) plotted against the long-eccentricity (405-kyr) phase. Inner circle: phasing of transgressive-regressive surfaces; TRmax = maximum transgression (base of the regressive tract), REGmax = maximum regression, oa = onset of aggradation (base of the lowstand systems tract). Outer circle: inferred eustatic sea-level maxima and minima. Blue and red arrows indicate the phase differences between transgressive-regressive extremes and eustatic sea-level forcing inferred from stratigraphic models (Supplementary materials, Table S6). Note that the rising phases of eustatic sea-level change (blue shading) are clustered close to the inflection point of rising eccentricity in both icehouse scenarios, whereas the opposite phasing is found in the greenhouse example.

405-kyr eccentricity vs. CTB [1] [kyr]				TR-REG vs. 405-kyr eccentricity [kyr]			ESL vs. TR-REG [kyr]			ESL vs. 405-kyr eccentricity [kyr]		
no.	max	min	uncert. [2]	TRmax [3]	REGmax [4]	uncert. [5]	ESLmax [6]	ESLmin [7]	uncert. [8]	ESLmax [6]	ESLmin [7]	uncert. [5]
230	890		±70	80		±60	81		±14	161		±62
		688	±69		196	±60		65	±22		261	±64
231	486		±68	110		±52	81		±14	191		±54
		284	±69		200	±58		65	±22		265	±62
232	82		±70	54		±66	81		±14	135		±67

[1]) CTB = Cenomanian/Turonian boundary
[2]) 2σ uncertainty relative to CTB (includes uncertainty in the location of CTB; Laurin et al. 2021)
[3]) TRmax = transgressive maximum; the maximum landward extent of shoreface siliciclastics (positive value = lag of TRmax behind 405-kyr max)
[4]) REGmax = regressive maximum; the maximum basinward extent of shoreface siliciclastics (positive value = lag of REGmax behind 405-kyr min)
[5]) 2σ uncertainty relative to 405-kyr maxima and minima (uncertainty of the 405-kyr metronome relative to CTB not included)
[6]) ESLmax = maximum in eustatic sea level (positive value = lag of ESLmax behind TRmax or 405-kyr max)
[7]) ESLmin = minimum in eustatic sea level (positive value = lag of ESLmin behind REGmax or 405-kyr min)
[8]) 2σ uncertainty relative to TRmax and REGmax (section 3.3)

Table 1. Timing of eccentricity cycles, transgressive-regressive shoreline movements (TR-REG) and inferred eustatic sea-level change (ESL); lower to lower middle Turonian, Bohemian Cretaceous Basin. The timing of 405-kyr extremes relative to local stratigraphy and Cenomanian-Turonian boundary is based on the “nominal” age model of Laurin et al. (2021).